THE ASTROPHYSICAL JOURNAL, 457:244–252, 1996 January 20

COOLING, SPUTTERING, AND INFRARED EMISSION FROM DUST GRAINS IN FAST NONRADIATIVE SHOCKS

ELI DWEK,[1] SCOTT M. FOSTER,[2] AND OLAF VANCURA[3]
Received 1994 August 24; accepted 1995 July 27

ABSTRACT

We model the dynamics, the destruction by sputtering, and the infrared (IR) emission from collisionally heated dust grains in fast ($\geq$400 km s^{-1}) astrophysical shocks in order to develop IR diagnostics for the destruction of grains in these environments. The calculations take into account the feedback from sputtering and IR emission on the gas-phase abundances, the cooling, and the ionization and thermal structure of the shock.

Sputtering changes the initial grain size distribution, creating a deficiency of small (radius $<$50 Å) grains compared to their preshock abundances. The altered grain size distribution depends on shock velocity and the density of the interstellar medium. Dust particles with sizes below $\approx$300 Å are stochastically heated, undergo temperature fluctuations, and radiate an excess of near-infrared emission ($\lambda \leq 40$ μm) over that expected for grains in thermal equilibrium. This near-infrared excess is a measure of the abundance of small grains and therefore a powerful diagnostic for the amount of destruction the grains were subjected to in the shock. We present here IR spectra from collisionally heated dust for a variety of shocks, and depict the changes in the spectra as a function of postshock column density. Our studies compliment those of Vancura et al. that examined the effects of the release of the sputtered refractory elements on the ultraviolet and X-ray emission. Multi-wavelength observations at X-ray, UV, and IR wavelengths are therefore essential in piecing together a comprehensive picture of the physics of grain destruction in fast astrophysical shocks.

Subject headings: dust, extinction — infrared: ISM: continuum — radiation mechanisms: thermal — shock waves

1. INTRODUCTION

Dust grains play an important role in determining the total energy balance in the interstellar medium (ISM), converting most of the galactic starlight to infrared (IR) emission, and heating clouds through the emission of photoelectrons. Equally important is their destruction, which recycles condensable elements from the solid back to the gaseous phase of the interstellar medium (ISM). On a galactic scale, it regulates the depletions of various refractory elements in the interstellar medium (Dwek & Scalo 1979, 1980; McKee 1989), and on a local scale, it affects the ionization structure of the shock (Itoh 1989), as well as the infrared (IR), the ultraviolet (UV), and the X-ray signature of the shocked gas (Vancura et al. 1994).

There is, however, only circumstantial evidence for the destruction of grains in fast shocks, all inferred from *IRAS* observations of young supernova remnants (see review by Dwek & Arendt 1992). In Cas A, the disparity between the mass of X-ray–emitting gas inferred from the IR observations (assuming a galactic dust-to-gas mass ratio) and that inferred from the X-ray observations can be taken as evidence for grain destruction in this remnant (Dwek et al. 1987). In Puppis A, comparison of the IR emission from a preshocked molecular cloud and that from a shocked X-ray–emitting region suggests a depletion in the population of small grains in the latter, presumably owing to the effect of grain destruction (Arendt, Dwek, & Petre 1991). In the Cygnus Loop, Arendt, Dwek, & Leisawitz (1992) decomposed the IR emission from the remnant into components that are associated with the optical and X-ray–emitting regions of the remnant. The IR emission from the hot X-ray gas does not exhibit the short-wavelength emission characteristic of small grains, presumably because of their destruction in this gas component.

In this paper we construct models for the IR emission in dusty nonradiative shocks which can be used to infer the occurrence of grain destruction in these shocks. Similar spectra were presented by Draine (1981); however, major new aspects of the present study are the inclusion of the effect of dust temperature fluctuations in modeling the IR emission, and the emphasis on grain dynamics and destruction and their effect on the evolution of the IR emission from the shocked gas. We will only consider the effects of grain destruction by sputtering, which is the dominant grain destruction mechanism in the high-velocity shocks considered in this paper. Grain-grain collisions become important only in low-velocity radiative shocks, in which sputtering is significantly suppressed because of the low gas temperatures and grains are accelerated to high velocities by the betatron acceleration mechanism (Shull 1977, 1978; see review by Draine & McKee 1993, and Tielens et al. 1994 and Jones et al. 1994 for more recent work).

Sputtering changes the initial grain size distribution, depleting the population of small grains in the initial grain size distribution. Small dust particles with sizes below $\approx$300 Å are stochastically heated, undergo temperature fluctuations, and radiate an excess of near-infrared emission ($\lambda \leq 40$ μm) over that expected for grains in thermal equilibrium. This near-infrared excess is a measure of the abundance of small grains and therefore a powerful diagnostic for the amount of destruction the grains were subjected to in the shock.

In § 2, we discuss the various physical processes that determine the behavior of the dust particles behind the shock. These include the effects of grain charging, collisional heating, and

[1] Code 685, Infrared Astrophysics Branch, NASA Goddard Space Flight Center, Greenbelt, MD 20771; edwek@stars.gsfc.nasa.gov.
[2] Astronomy Department, University of Maryland, College Park, MD 20742. Current address: NRAO, P.O. Box 0, Socorro, NM 87801.
[3] Center for Astrophysics, 60 Garden Street, Cambridge, MA 02138.

destruction by sputtering. Particular emphasis is placed on the dynamics of the dust behind the shock. Proper treatment of the dynamics enables us to calculate the abundance of the sputtered atoms as a function of their post-shock position, an important input for calculating the effects of grain destruction on the ionization state, the thermal structure, and the IR and X-ray emissivity throughout the shock. In calculating the grain destruction by sputtering, we use more recent fits to experimental data and find that the thermal sputtering rate is slightly enhanced compared to earlier results by Draine & Salpeter (1979). Similar conclusions were reached by Tielens et al. (1994), who used the same sputtering formalism used in this paper. The shock code used in the model and the numerical implementation of the grain processes are described in § 3. They are practically identical to those described by Vancura et al. (1994). In § 4 we present detailed results for a 400 km s^{-1} shock, expanding into a medium with a total number density of $n_0 = 0.1$ cm^{-3}. A comparison of the amount of grain destruction, and resulting IR signature for a grid of shock velocities and ISM densities, is presented in § 5. The results of our paper are then briefly summarized in § 6.

2. GRAIN PHYSICS

2.1. *Grain Dynamics*

The passage of a shock through a stationary parcel of gas and dust will set up a relative gas-dust motion with an initial velocity of $\frac{3}{4}V_{\rm shock}$, where $V_{\rm shock}$ is the shock velocity relative to the unperturbed interstellar medium. In the absence of any magnetic field, the dust particles will move ballistically through the postshock gas, gradually coming to rest with respect to the shocked gas as a result of collisional drag. However, in the presence of a magnetic field the dust particles will execute a complex motion behind the shock, which can be considerably simplified when the grain's Larmor radius, $R_{\rm L}$, is small compared to some characteristic scale length of a shocked parcel of gas (Spitzer 1976). The dust particles will then be effectively coupled to that parcel of gas, executing a gyromotion with an initial velocity of $\frac{3}{4}V_{\rm shock}$ around the magnetic field lines. Since the magnetic field is effectively frozen into the gas, any compression of the gas will be accompanied by an equal compression in the number density of dust particles.

The Larmor radius of a dust grain of radius a gyrating around a magnetic field B is given by (e.g., Spitzer 1978) $R_{\rm L} = m_d w_d c/Q_{\rm gr} B$, where $m_d = (4/3)\pi a^3 \rho$, is the mass of the dust grain, ρ is its mass density, w_d is its velocity relative to the gas (initially equal to $\frac{3}{4}V_{\rm shock}$), and $Q_{\rm gr}$ is its charge. The grain charge is determined by the combined effect of collisional charging, photoelectric, and secondary electron emission (Spitzer 1978; McKee et al. 1987), and in plasmas with temperatures above $\sim 10^6$ K the dimensionless potential parameter, ϕ, is simply given by (McKee et al. 1987) $\phi = eQ_{\rm gr}/akT \approx 10^5/T$ where T is the gas temperature, giving $Z_{\rm gr} \equiv Q_{\rm gr}/e \approx 6 \times 10^3 a(\mu{\rm m})$. In practical units, $R_{\rm L}$ is given by (see also Shull 1977):

$$R_{\rm L}({\rm cm}) = 7.85 \times 10^{19} \frac{a^3(\mu{\rm m}) w_d({\rm km\ s^{-1}})}{Z_{\rm gr} B(\mu{\rm G})}$$

$$\approx 1.3 \times 10^{16} \frac{a^2(\mu{\rm m}) w_d({\rm km\ s^{-1}})}{B(\mu{\rm G})}, \quad (1)$$

where we took the grain mass density $\rho = 3$ g cm^{-3}. In general, the dust particles are well coupled to the gas, but for high shock velocities the Larmor radius may be larger than Δx, the size of a resolution element in the postshock flow. However, even if the grains are initially not coupled to the gas and $R_{\rm L} \geq \Delta x$, drag forces will slow them down so that $R_{\rm L} \ll \Delta x$ at some velocity $w_{\rm cp}$. We consider a dust particle to be coupled to the gas when it can complete a full gyration within a single parcel of gas length Δx, that is, when $2R_{\rm L} \leq \Delta x$. The velocity $w_{\rm cp}$ below which a dust grain is considered coupled to the gas is then given by

$$w_{\rm cp}({\rm km\ s^{-1}}) = 4 \times 10^{-17} \frac{B(\mu{\rm G})\Delta x({\rm cm})}{a^2(\mu{\rm m})}. \quad (2)$$

The deceleration of a dust particle is given by (e.g., Dwek & Arendt 1992)

$$\frac{dw}{dt} = \frac{F_{\rm drag}}{(4/3)\pi a^3 \rho}$$

$$= -\frac{3n\mu m_{\rm H} w_d^2}{4a\rho} [\gamma G_{\rm coll}(S) + G_{\rm plasma}(Z, \phi, n_e, S)], \quad (3)$$

where $F_{\rm drag}$ is the collisional drag force on the dust, n is the number density of the impinging dust particles, μ is their atomic weight, $m_{\rm H}$ is the hydrogen mass, γ is a factor between 0.5 and 1 (we used $\gamma = 0.5$), and $G_{\rm coll}$ is the thermal correction to the collisional drag force given by

$$G_{\rm coll}(S) = \left[\pi^{-1/2}\left(\frac{1}{S} + \frac{1}{2S}\right)e^{-S^2} + \left(1 + \frac{1}{S^2} - \frac{1}{4S^4}\right) {\rm erf}\,(S)\right], \quad (4)$$

where $S^2 = (\mu m_{\rm H} w_d^2)/2kT$, and erf is the error function. $G_{\rm plasma}$ is the drag force resulting from the cumulative effect of small-angle Coulomb scattering (Spitzer 1962), which turns out to be negligible for the shock velocities considered here. The deceleration is inversely proportional to the grain radius. As a result, the smaller grains will slow down shortly after passing the shock front, while the larger grains will continue to move ballistically throughout the shocked gas.

Grains that move ballistically through the postshock gas can be regarded as a separate fluid. The number density $n_d(a, x)da$ of grains with radii between a and $a + da$ at any position x behind the shock is given by the continuity equation

$$n_d(a, x)da\, u_d(a, x) = n_d(a_0, 0)da_0 V_{\rm shock} = {\rm constant}. \quad (5)$$

where $a_0 = a(x) + \Delta a_{\rm sput}(x)$ is the initial grain radius at $x = 0$, $\Delta a_{\rm sput}(x)$ is the accumulative change in grain radius resulting from sputtering at distance x, $u_d(a, x)$ is the grain velocity relative to the shock front, and where $da = da_0$, since the change in grain radius $\Delta a_{\rm sput}$ is independent of the initial grain size (see § 2.2). As u_d decreases, the number density of dust grains increases. Eventually, the grains are slowed down to the point where $w_d \leq w_{\rm cp}$. At this point, Larmor gyration effectively couples the dust to the gas, and the number density of dust particles per H-atom will remain constant as long as $a > 0$, that is, the grain is not completely destroyed.

2.2. *Grain Destruction*

The sputtering rate of a dust particle moving at a velocity w_d through a thermal gas of particles of mass m, temperature T,

and number density n is given by (Draine & Salpeter 1979)

$$R = \pi a^2 n\left(\frac{8kT}{\pi m}\right)^{1/2}\frac{e^{-S^2}}{2S}\int_{\epsilon_{th}}^{\infty}\epsilon^{1/2}\left(1-\frac{\phi}{\epsilon}\right) \times e^{-\epsilon}\sinh(2S\epsilon^{1/2})Y[E=(\epsilon-\phi)kT]d\epsilon\,, \quad (6)$$

where $S^2 = mw_d^2/(2kT)$, $\epsilon = E/kT$, $Y(E)$ is the angle-averaged sputtering yield at incident projectile energy E, and ϵ_{th} is the sputtering threshold, E_{th}, in units of kT. In calculating the sputtering yield, we followed the procedure of Tielens et al. (1994); that is, we used the sputtering yield formulae of Sigmund (1981), modified by two correction terms that extended the energy dependence of yields to energies close to the threshold regime (Bodhansky 1984).

Figure 1 shows the rate of change of radius normalized to the H number density, for spherical graphite and silicate grains as a result of sputtering by hydrogen, helium, and CNO ions, as a function of gas temperature. We assumed cosmological relative abundances (Anders & Grevesse, 1989; Table 1), for which $n_{He}/n_H = 0.097$ cm^{-3}, and $n_{CNO}/n_H = 0.0013$ cm^{-3}. The solid lines represent the rates for dust particles that are stationary with respect to the hot gas. The relative contributions of the various ions to the sputtering rate are determined by their relative yields and collision rates. Sputtering by protons dominates the yield at all temperatures, in spite of the fact that their sputtering yield is the lowest. At temperatures above $\sim 3 \times 10^6$ K, the sputtering rate is nearly constant, the increase in the flux of incident particles being cancelled out by the increased transparency of the dust to the incoming particles, and is to within a factor of 2 given by

$$\frac{1}{n_H}\frac{da}{dt} \approx 1 \times 10^{-6}\ \text{cm}^3\ \mu\text{m yr}^{-1} \quad \text{for graphite grains } (T \geq 3 \times 10^6\ \text{K}$$

and by (7)

$$\frac{1}{n_H}\frac{da}{dt} \approx 2 \times 10^{-6}\ \text{cm}^3\ \mu\text{m yr}^{-1} \quad \text{for silicate grains } (T \geq 3 \times 10^6\ \text{K})\,,$$

The sputtering rate increases when the dust is in motion, and to illustrate this effect we also included the rate for a dust particle that is moving at a velocity of 100 km s^{-1} with respect to the hot gas. At temperatures below $\sim 10^5$ K, all the sputtering is caused by the relative gas-grain motion, and the sputtering rate is now dominated by the impinging He ions. The rate approaches a constant, since almost all the energy of the collision originates from the motion of the dust grain through the gas. In the limit of $S \to \infty$, the sputtering rate for $E > E_{th}$ is given by

$$R = \pi a^2 n w_d\, Y(E = \tfrac{1}{2}mw_d^2)\,. \quad (8)$$

2.3. *Infrared Emission from Grains*

The infrared spectrum of a single dust grain of radius a is given by

$$I_\nu(a) = 4\pi a^2\int_0^\infty B_\nu(T)Q_\nu(a)P(a,t)dT\,, \quad (9)$$

where $B_\nu(T)$ is the Planck function at temperature T, $Q_\nu(a)$ is the dust emissivity at frequency ν, and $P(a, T)dT$ is the probability of finding the grain in the temperature interval $T \to T + dT$.

Dust grains embedded in a plasma will undergo temperature fluctuations when the heat capacity of the dust grain is small enough that a single electronic collision can cause a large surge in the grain temperature, and when the cooling time following a temperature surge is short compared to the average time between collisions (Dwek 1986). Calculations of $P(T)$ show that the population of dust particles undergoing temperature fluctuations in shocks is significantly larger than that residing in diffuse clouds and heated by the general interstellar radiation field. For a 400 km s^{-1} shock expanding into a medium with $n_H = 0.1$ cm^{-3}, temperature fluctuations are still important for 0.05 μm radii dust particles, compared to 0.02 μm for dust in diffuse clouds (Draine & Anderson 1985).

Larger grains will radiate at an equilibrium grain temperature T_{eq}, determined by the equation

$$4\pi a^2\int_0^\infty \pi B_\nu(T_{eq})Q_\nu(a)d\nu = H(a, u_d, T_{gas})\,, \quad (10)$$

where $H(a, u_d, T_{gas})$ is the collisional heating rate given, for example, by Dwek & Arendt (1992). For dust radiating at the equilibrium temperature T_{eq}, the IR spectrum is given by equation (9) with $P(a, T) = \delta(T - T_{eq})$, a delta function at the size-dependent equilibrium dust temperature.

Total IR intensities from a shock were obtained by integrating the emission from the various individual grains over

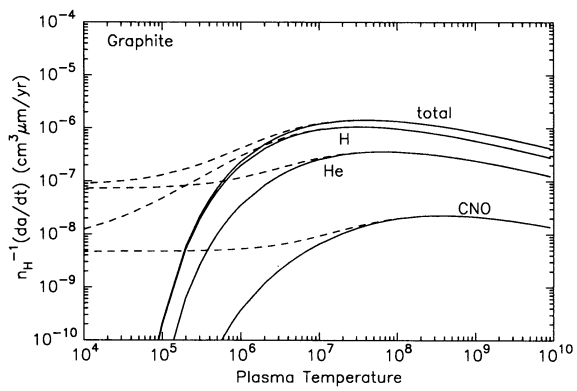

FIG. 1a

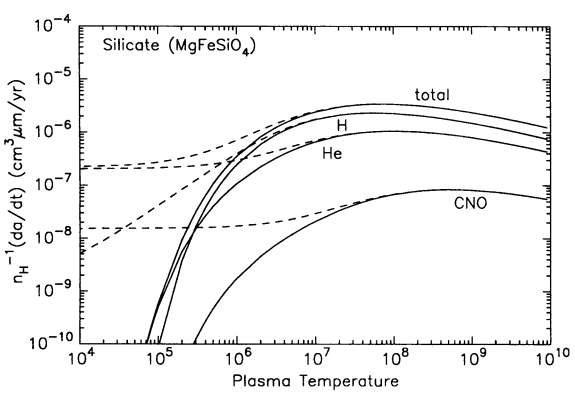

FIG. 1b

FIG. 1.—Rate of change of grain radius for (*a*) spherical graphite and (*b*) silicate ($MgFeSiO_4$) grains at rest (*solid lines*) and moving through a plasma at 100 km s^{-1} (*dashed lines*) as a result of sputtering by H, He, and CNO ions as a function of plasma temperatures. Rates are normalized to the H number density and the relative abundances of He, and CNO ions were taken from Table 1 (undepleted abundances).

postshock column densities until the shock was truncated (see discussion in § 3.4 below). The fluxes reported here represent the flux emerging from a unit surface area (in cm^2) of a plane-parallel shock that is viewed face on, i.e.,

$$F_\nu = \int_0^{l_{tr}} \frac{n_d(a, l)}{n_H(l)} I_\nu(a, l) dl , \quad (11)$$

where l is the post shock H column density, l_{tr} is the column density at which the shock was truncated, and $I_\nu(a, l)$ is the single dust spectrum (eq. [9]) at column density l. Fluxes need to be multiplied by a factor of $\Omega/4\pi$ to account for the beam size Ω.

3. NUMERICAL IMPLEMENTATION

3.1. *The Shock Model*

The shock code used in this paper is the one developed by Raymond (1979) with subsequent improvements by Cox & Raymond (1985) and Long et al. (1992). We have coupled this code to a number of routines that for a given set of plasma parameters calculate the amount of grain destruction, update the gas phase abundances of the heavy elements, and calculate the contribution of gas-grain collisions to the cooling of the gas. The implementation is similar to that of Vancura et al. (1994), except that we also follow in more detail the dynamics and abundance of the dust in the postshock flow.

Model results are presented for a grid of shock velocities: 400, 600, 800, 1000, 1500, and 2000 km s^{-1}, expanding into media with preshock H intensities of 0.1, 1, 10, and 100 cm^{-3}. All models assume a preshock magnetic field of 1 μG and that the hydrogen is 30% pre-ionized (Vancura et al. 1994). The fact that the hydrogen is not fully ionized before it is shocked causes an initial surge in the cooling rate of the gas but has a negligible effect on the subsequent postshock density and temperature structure because of the high velocities considered in this paper. We also assumed that the electron and ion temperatures are instantly equilibrated behind the shock. Relaxing this assumption may, in principle, affect the IR emission, since the dust is primarily heated by electrons, whereas its destruction proceeds primarily through ionic collisions. However, the studies of Vancura et al. (1994) showed that the difference in the sputtered mass and IR emission between shock models that assumed Coulomb or instant equilibration between the electron and ion temperatures was small. For each velocity-density pair, we calculated two models, one with undepleted gas phase abundances, and the other with select refractory elements locked up in dust. Table 1 shows the assumed gas phase abundances for each model.

3.2. *The Dust Model*

The refractory elements that were depleted from the gas phase were placed in two dust populations. Depleted carbon went into graphite grains, and all other depleted elements (O, Mg, Si, and Fe) were assumed to be in silicate grains composed of Mg Fe SiO_4. Both populations were characterized by an a^{-k} grain size spectrum in the a_{min} to a_{max} radius interval, with $k = 3.5$, $a_{max} = 0.25$ μm (Mathis, Rumpl, & Nordsieck 1977), and $a_{min} = 3$ Å. The size spectrum was normalized so that the total mass of the dust was equal to the total mass of the depleted elements in the preshock gas.

In calculating the collisional heating rate of the dust, we took the numerical approximations to the electron ranges in the solid from Dwek & Smith (1996), and those for H, He, and CNO nuclei from Draine & Salpeter (1979). Optical constants for calculating the grain emissivities were taken from Draine & Lee (1984). In calculating the sputtering rate, we adopted a surface binding energy U_0 of 7.5 eV for graphite grains and 5.7 eV for silicates. Grain mass densities were taken to be 2.2 and 3.3 g cm^{-3} for graphite and silicates, respectively.

TABLE 1

GAS-PHASE ABUNDANCES OF SELECT ELEMENTS[a]

Element	Undepleted Abundance[b]	Depleted Abundance[c]
He	10.99	10.99
C.....	8.56	8.04
N	8.05	8.05
O	8.93	8.86
Ne	8.09	8.09
Mg.....	7.58	6.81
Si	7.55	6.59
S	7.26	7.26
Ar.....	6.56	6.56
Ca	6.34	6.34
Fe.....	7.51	5.51
Ni.....	6.25	6.25

[a] Scaled to log (H) = 12.
[b] Anders & Grevesse 1989.
[c] De Boer, Jura, & Shull 1987.

3.3. *Assumptions and Approximations*

At each distance x, or time t behind the shock, we update the physical parameters of the dust from the previous step, $x - \Delta x$, and we calculate the infrared emission and the amount of refractory material that is returned to the gas phase. The calculations are complicated by the fact that the grain deceleration and destruction rates are coupled. However, the change in grain radius as it travels a distance Δx behind the shock is small enough that we can first solve for its new velocity at x for the original grain radius at $x - \Delta x$. Sputtering rates are then calculated at the velocity $v = \frac{1}{2}[v(x - \Delta x) + v(x)]$. Sputtered atoms are assumed to be neutral. From the sputtering rate and grain velocity, we calculate the amount of grain destruction in the $x - \Delta x$ to x interval, calculate Δa_{sput}, the cumulative change in grain radius since it was swept up by the shock, and update the grain size distribution. We then calculate the Larmor radius of each dust particle and compare it with the scale length of the resolution element Δx. If $2R_L(a) > \Delta x$, the dust particle is assumed to be ballistic, and the number density of dust grains at x is determined from equation (5). If $2R_L(a) \leq \Delta x$, the particle is assumed to be coupled to the gas and its number density, $n(a)da$, in the $a - a + da$ size interval is proportional to the H number density in that parcel of gas. The proportionality constant is determined by the $n(a)da$–to–n_H ratio in the previous step. Finally, we calculate the collisional heating rate for the grain population in this parcel of gas, which should equal the IR emission rate.

Calculations of the IR emission from each parcel of gas are complicated by the stochastic nature of the dust heating, which makes the problem computationally too time consuming. Fortunately, for the shock velocities considered here, the postshock flow is nearly isothermal and has an almost constant density profile, until cooling becomes important. This is illustrated in Figure 2, which shows the temperature and density profiles of the shock models characterized by $V_{shock} = 400$ km s^{-1} and $n_0 = 0.1$ cm^{-3}. Therefore, we can adopt a single

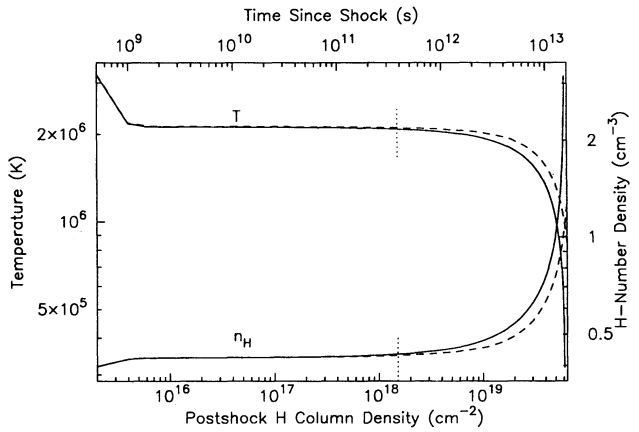

FIG. 2.—Postshock temperature and density profiles as a function of hydrogen column density and time since shock passage for a 400 km s^{-1} shock propagating into a dusty medium (*solid lines*) and a dust-free medium (*dashed lines*) with an ambient total gas number density of $n_0 = 0.1$ cm^{-3}. The dotted line shows the column density at which the shock was truncated in order to simulate a Sedov blast wave.

column density–averaged temperature and density for the entire shock region up to some cutoff x_f and calculate the IR spectrum emerging from this region. To utilize this simplification, we have to ignore the effect of the grain velocity, which varies throughout the postshock region, in calculating the dust temperature. This approximation will create a discrepancy between the calculated energy loss by gas-grain collisions, where the relative gas-grain motion was taken into account, and the calculated energy lost by IR emission, where this effect was ignored. Fortunately, this discrepancy is small (<10%), since grain heating is dominated by collisions with electrons, whose thermal velocity is much higher than the grain velocity. From the dust temperature (or temperature distribution, if it is stochastically heated), we calculate the infrared spectrum emitted by a single dust grain for each grain in our size grid.

3.4. *Truncation of the Shock Models*

In order to calculate the total infrared spectrum from a shock, we need to truncate the shock at some appropriate time or distance and sum up the individual spectra from all the grains in the postshock region. Since these fast shocks are intended to represent expanding supernova blast waves, it is appropriate to choose a cutoff time that is related to the age of a remnant that has decelerated to the velocity of the shock under consideration. The temperature and density profiles of the blast wave will, however, differ from those of a plane-parallel shock. Examination of the gas density and temperature profiles of a Sedov-Taylor blast wave (e.g., Taylor 1950) shows that they deviate from that of a plane-parallel shock only in the inner 70% of the radius of the blast wave, which contains only a small fraction (~8.2%) of the swept-up mass. The time required for a parcel of gas to travel across the outer 30% of the shock is equal to $\frac{2}{5}t_{SN}$, where t_{SN}, the age of the blast wave, is given by (e.g., Spitzer 1978)

$$t_{SN} = \left(\frac{2}{5}\xi_0\right)^{5/3}\left(\frac{E_0}{\mu m_H n_0}\right)^{1/3} V_{shock}^{-5/3}, \quad (12)$$

where $\xi_0 = 1.17$ for $\gamma = 5/3$, $\mu \approx 1.4$ is the mean molecular weight of the gas, m_H is the mass of a hydrogen atom, n_0 is the density of the ambient gas, and V_{shock} is the present shock velocity. Choosing a value of $E_0 = 10^{51}$ ergs for the initial energy of the blast, we find that the value of the cutoff time is

$$t_{cutoff} = \frac{2}{5}t_{SN}(E_0 = 10^{51}\ \text{ergs}, V_{shock}, n_0)$$

$$= 1.2 \times 10^3\left(\frac{E_{51}}{n_0}\right)^{1/3} V_3^{-5/3}\ \text{yr}, \quad (13)$$

where E_{51} is the initial blast-wave energy in units of 10^{51} ergs, and V_3 is the shock velocity in 10^3 km s^{-1}.

4. RESULTS FOR $V_{shock} = 400$ km s^{-1} AND $n_0 = 0.1$ cm^{-1}

Our models reveal a number of important characteristics of dusty shocks. Throughout this section, we will illustrate many of these characteristics with a representative shock model, $V_{shock} = 400$ km s^{-1}, $n_0 = 0.1$ cm^{-3}. Only final results will be presented for the full grid of shock models. In each of the plots of this model, a vertical dotted line will mark the time (or column density) at which we truncated the shock.

4.1. *The Effect of Dust on Shock Structure*

Figure 2 shows the temperature and density structure for a typical shock model both with dust (*solid lines*) and without dust (*dashed lines*). The sudden cooling and compression immediately behind the shock is the result of hydrogen ionization. Once the hydrogen is ionized, the temperature and density level off until significant cooling sets in. In this region, we can approximate the plasma temperature and density as a constant, allowing us to model dust temperature fluctuations. Figure 3 shows the cooling of the shock caused by dust and all other cooling mechanisms. Note that once the neutral hydrogen is ionized, the dominant gas cooling mechanism is the infrared emission from the dust. This typically lasts until the dust is destroyed. The main result of the addition of dust to the shock model is that the extra cooling causes the shock to become radiative sooner.

4.2. *Evolution of the Grain Size Distribution*

Figures 4 and 5 depict the destruction of the dust in two different ways. Figure 4 shows the fractional mass of the dust that is returned by sputtering to the gas, as a function of

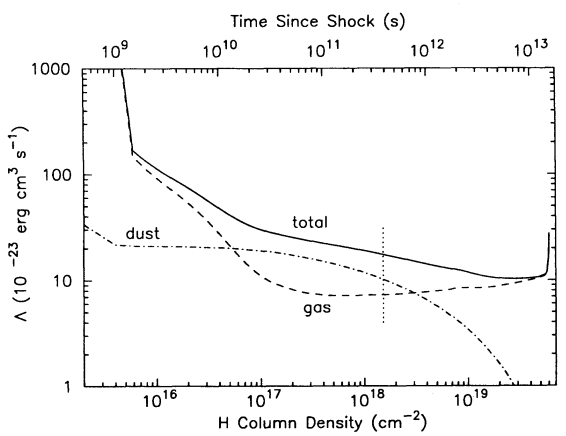

FIG. 3.—The cooling rate of the postshock gas resulting from gas-grain collisions (marked "dust") and atomic processes (marked "gas") as a function of hydrogen column density and time since shock passage for a 400 km s^{-1} shock propagating into a dusty medium with a value of $n_0 = 0.1$ cm^{-3}. The dotted line shows the column density at which the shock was truncated.

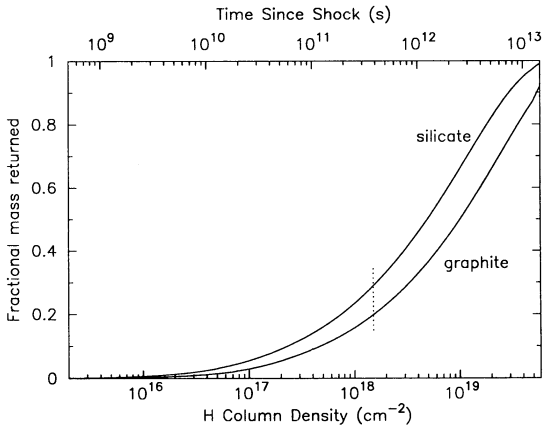

FIG. 4.—Mass fraction of dust material returned to the gas as a function of hydrogen column density and time since shock passage as a result of sputtering behind a 400 km s^{-1} shock propagating into a dusty medium with a preshocked density of $n_0 = 0.1$ cm^{-3}. The dotted line shows the column density at which the shock was truncated.

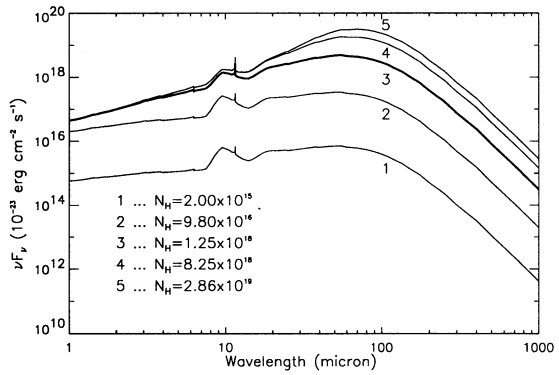

FIG. 6.—Infrared spectra integrated to various hydrogen column densities for a 400 km s^{-1} shock propagating into a dusty medium with an ambient gas number density of 0.1 cm^{-3}. At column densities above $\sim 10^{18}$ cm^{-2}, the short-wavelength emission ceases to contribute to the cumulative spectrum owing to the effect of grain destruction. The bold curve at $N_H = 1.25 \times 10^{18}$ cm^{-2} represents the grain size distribution at the column density at which the shock was truncated.

column density and time. In all shock models, the dust is almost completely destroyed by the time shock compression takes place at a column density of about 5×10^{19} cm^{-2}. However, the shock depicted in the figure is truncated at $N_H = 1.25 \times 10^{18}$ cm^{-2}, so that only 21% of the graphite and 29% of the silicates are returned to the gas phase.

Figure 5 shows the evolution of the grain size distribution for various values of N_H in units of 10^{18} cm^{-2}. Sputtering decreases the relative number of small grains. Since the small dust grains undergo temperature fluctuations and produce the short-wavelength excess emission, we expect to see a decline in this excess with increasing column density.

4.3. *Evolution of the Infrared Spectrum*

Figure 6 shows the infrared spectrum from our sample shock integrated to various column densities. As we integrate to larger column densities, the short-wavelength excess does not increase as rapidly as the rest of the spectrum because of the destruction of the small dust grains as shown in Figure 5. This point it illustrated in Figure 7, where we plot the ratio of the 5 μm flux to the 100 μm flux and the ratio of the 25 μm to 100 μm flux normalized to their immediate postshock values. In both cases, the short-wavelength flux drops significantly relative to the long-wavelength flux. This is especially true for the 5 μm flux, which is almost entirely the result of temperature fluctuations in small grains.

5. COMPARISON BETWEEN THE VARIOUS SHOCK MODELS

5.1. *Grain Destruction*

Figures 3 and 4 show the important role that the cutoff time plays in determining the fractional mass of dust that is destroyed by the shock. Almost all the dust is destroyed by $N_H = 5 \times 10^{19}$ cm^{-2}, but only $\sim$20%–30% of the dust is destroyed by the cutoff time. Truncating the shock at time $t = \frac{2}{5} t_{SN}$ decreases the amount of grain destruction with increasing shock velocity. This seemingly contradictory situation is simply a result of the fact that the higher velocity shocks are younger. Since the destruction rate is fairly insensitive to shock velocity at $V_{shock} > 400$ km s^{-1}, the age of the shock determines the amount of sputtered material. An example is Cas A, an $\sim$300 yr old remnant that decelerated to a velocity of $\sim$1800 km s^{-1}, in which at least $\sim$30% of the

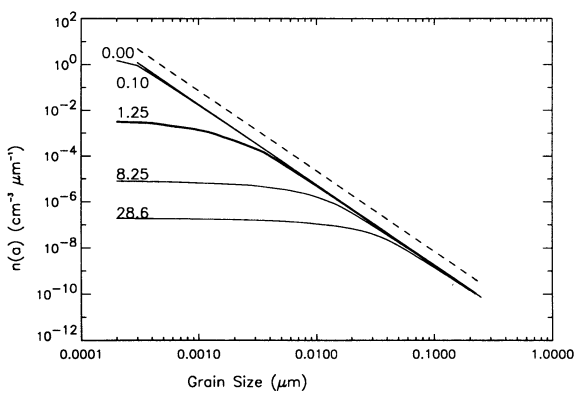

FIG. 5.—Graphite grain size distribution function, $n(a)$, at various hydrogen column densities N_H (in units of 10^{18} cm^{-2}), for a 400 km s^{-1} shock propagating into a dusty medium with $n_0 = 0.1$ cm^{-3}. The bold curve at $N_H = 1.25 \times 10^{18}$ cm^{-2} represents the grain size distribution at the column density at which the shock was truncated.

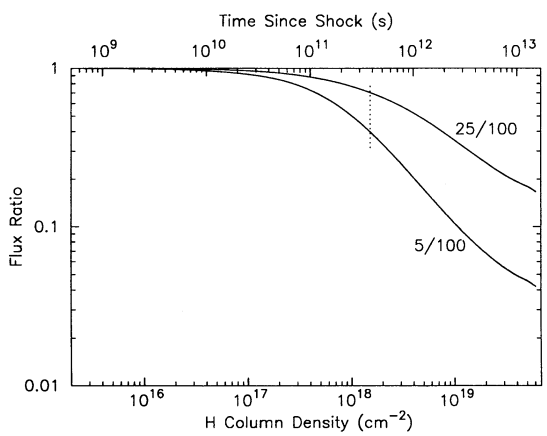

FIG. 7.—Evolution of 25 μm/100 μm and 5 μm/100 μm flux ratios normalized to their immediate postshock value behind a 400 km s^{-1} shock propagating into a dusty medium with $n_0 = 0.1$ cm^{-3}. The 5 and 25 μm fluxes decrease rapidly as a function of time due to the effect of grain destruction. The dotted line shows the column density at which the shock was truncated.

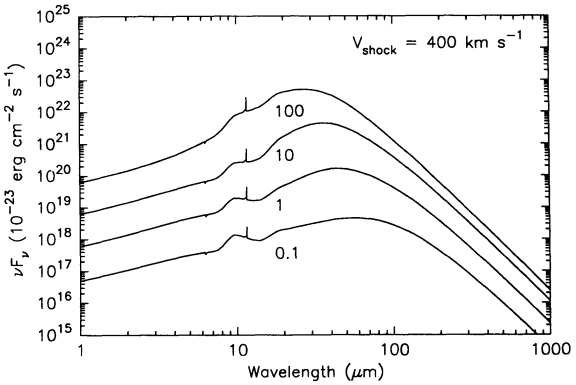

FIG. 8*a*

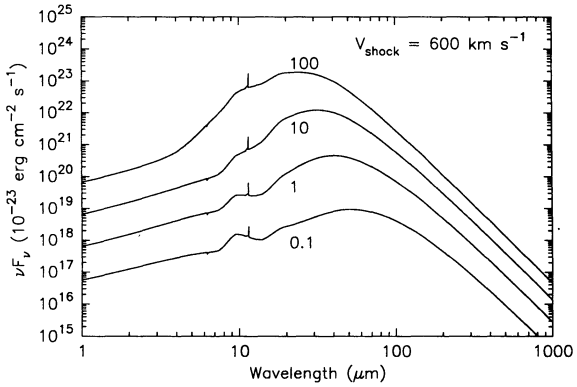

FIG. 8*b*

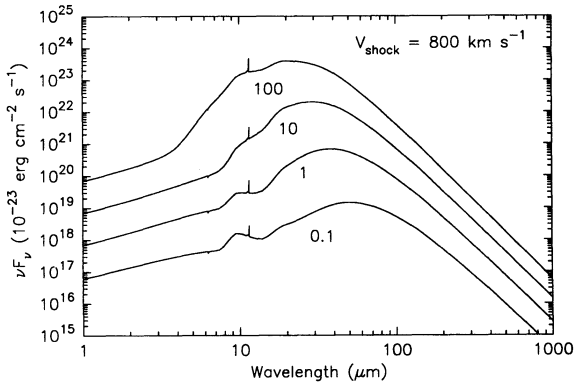

FIG. 8*c*

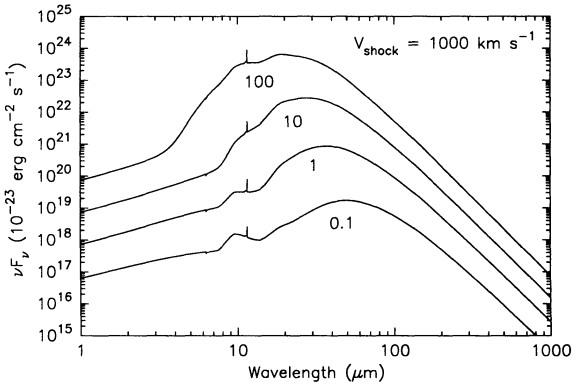

FIG. 8*d*

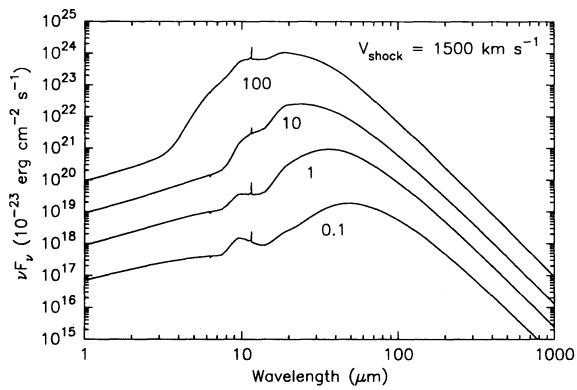

FIG. 8*e*

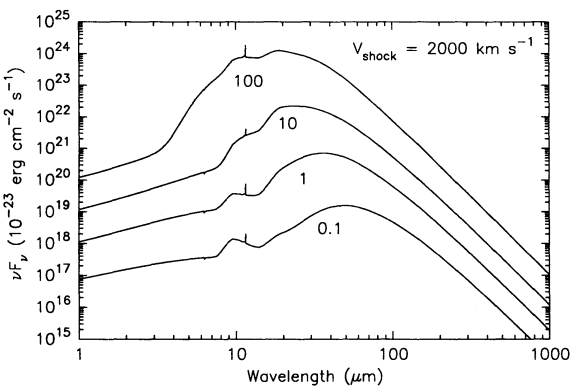

FIG. 8*f*

FIG. 8.—Model supernova spectra for (*a*–*f*) 400, 600, 800, 100, 1500, and 2000 km s^{-1} shocks propagating into dust media with gas densities n_0 = 0.1, 1, 10, and 100 cm^{-3}

grains survived to give rise to the observed IR emission (Dwek et al. 1987). At any given shock velocity, grain destruction increases with ISM density. Table 2 summarizes the total amount of dust destroyed by the cutoff time in each of the shock models explored in this paper.

5.2. *Comparative Infrared Spectra*

Figures 8*a*–8*f* show the effects of varying shock velocity and preshock gas density on the infrared shock spectra. These figures illustrate a few basic trends already pointed out by Draine (1981). First, for a given shock velocity, the peak of the emission, λ_{peak}, moves to shorter wavelengths and the total flux increases as a function of ISM density. Second, for a given ISM density, λ_{peak} moves to shorter wavelengths as the shock velocity increases. Both trends can be understood in terms of an increase in the gas-grain collision rate with gas temperature and density. The increased collision rate increases the total amount of cooling and increases the equilibrium grain temperature, shifting the emission spectrum to shorter wavelengths.

The main difference between our results and the spectra presented by Draine (1981) is the excess emission at short wavelengths from the stochastically heated dust particles. This additional short-wavelength emission component broadens

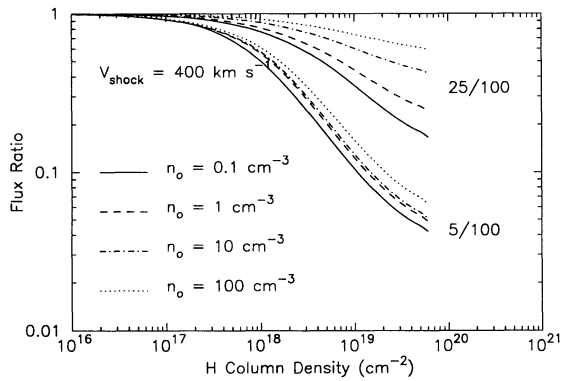

FIG. 9a

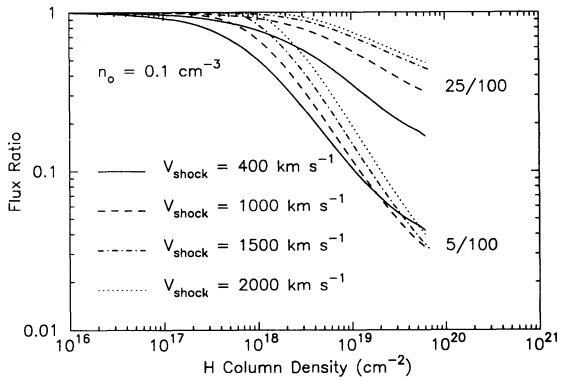

FIG. 9b

FIG 9.—Evolution of the 25 μm to 100 μm flux ratio and the 5 μm to 100 μm flux ratio as a function of postshock H column density: (*a*) for a 400 km s^{-1} shock propagating through an ISM characterized by various preshock densities; and (*b*) for shocks propagating with various velocities through an ISM with a density of $n_0 = 0.1$ cm^{-3}.

the spectrum, and the position of λ_{peak} is less well defined compared to the spectra which neglect the effect of dust temperature fluctuations.

Figure 9 shows the evolution of the normalized 25 μm to 100 μm and the 5 μm to 100 μm flux ratios as a function of postshock H column density for (*a*) a 400 km s^{-1} propagating through a various density media, and (*b*) for an ISM characterized by a preshock density of 0.1 cm^{-3} and various shock velocities. The 25 μm to 100 μm flux ratio is sensitive to the wavelength of the peak emission and therefore shows large variation between models. Most of the 5 μm flux, with the exception of the fastest, highest density shocks, arises from temperature fluctuations in small dust grains. As a result, there is not as much variation in the 5 μm to 100 μm flux between models. The relatively large drop in the 5 μm to 100 μm flux ratio as compared to the 25 μm to 100 μm flux ratio is explained by the fact that the 5 μm flux depends so strongly on the small grains which are the first to be destroyed.

TABLE 2

MASS FRACTION OF GRAINS DESTROYED AS A FUNCTION OF SHOCK VELOCITY AND PRESHOCK ISM DENSITY[a]

SHOCK VELOCITY (km s^{-1})	n_0 (cm^{-3})	MASS FRACTION OF GRAINS DESTROYED	
		Graphite	Silicate
400	0.1	0.21	0.29
	1.0	0.44	0.58
	10.0	0.78	0.92
	100.0	1.00	1.00
600	0.1	0.16	0.24
	1.0	0.36	0.49
	10.0	0.36	0.85
	100.0	0.99	1.00
800	0.1	0.13	0.20
	1.0	0.30	0.42
	10.0	0.61	0.77
	100.0	0.96	1.00
1000	0.1	0.10	0.16
	1.0	0.25	0.36
	10.0	0.53	0.69
	100.0	0.92	0.99
1500	0.1	0.07	0.11
	1.0	0.18	0.26
	10.0	0.40	0.54
	100.0	0.78	0.91
2000	0.1	0.05	0.08
	1.0	0.14	0.20
	10.0	0.32	0.44
	100.0	0.66	0.81

[a] Shocks were truncated at time $t = \frac{2}{3}t_{SN}(E_0 = 10^{51}$ ergs, $n_0)$; see text for details.

5.3. *A Shock Model Color-Color Diagram*

Figure 10 depicts the $R_{25/100} \equiv F(25\ \mu m)/F(100\ \mu m)$ versus $R_{5/100} \equiv F(5\ \mu m)/F(100\ \mu m)$ ratio for all shock models in a color-color diagram. If all the IR emission originates from dust radiating at the equilibrium dust temperature, then for a given ISM density, both flux ratios should increase with shock velocity, since the emission from both short wavelengths increases with dust temperature. This trend is depicted in the figure for $n_0 = 100$ cm^{-3}. On the other hand, if all the emission at wavelengths $\lambda < 30$ μm originates from stochastically heated dust, then both flux ratios should decrease with shock velocity, since then only the 100 μm emission, which originates from dust radiating at the equilibrium temperature, increases with shock velocity. This trend is depicted in the figure for $n_0 = 0.1$ cm^{-3}. Other density grouping show a combination of both trends, which illustrates the change in the origin of the short-wavelength emission (from equilibrium heated dust to stochastically heated dust) as a function of shock velocity.

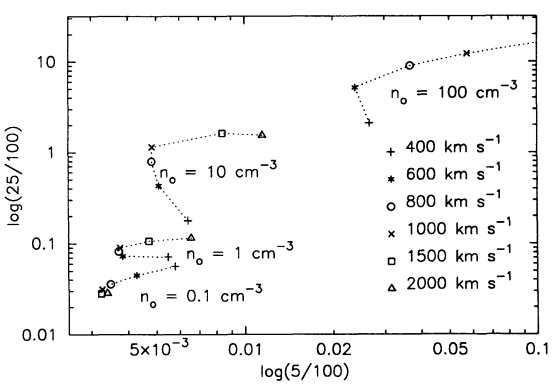

FIG. 10.—The $F(5\ \mu m)/F(100\ \mu m)$ is plotted vs. the $F(25\ \mu m)/F(100\ \mu m)$ flux ratio in a color-color diagram for all shock models considered in the paper. Dotted lines connect all shock models expanding into the same ISM density. A description of the figure is presented in the text.

6. SUMMARY

We calculated the destruction by sputtering of grains in fast nonradiative shocks. Sputtering rates for graphite and silicate dust are presented in Figures 1*a*–1*b*. The fractional mass of the dust destroyed as a function of shock velocity and ISM densities is presented in Table 2.

The effect of sputtering is to create a deficiency of very small particles compared to their preshock abundance. Figure 5 depicts the evolution of the grain size distribution as a function of postshock column density.

The progressive depletion of small grains as a function of column density affects the short-wavelength R emission which arises predominantly from the population of very small grains that is stochastically heated by the ambient hot gas. Figures 6 and 7 depict the changes in the short-wavelength ($\lambda < 40$ μm) emission as a function of postshock column density. Figure 10 is a color-color diagram illustrating the relative contribution of stochastically heated dust and dust radiating at the equilibrium dust temperature to the short-wavelength emission.

We conclude that observations of supernova remnants at wavelengths at which most of the emission arises from very small grains undergoing temperature fluctuations are important for studying grain destruction processes in shocks.

We thank John Raymond for the use of the shock code and for his comments on the manuscript. We acknowledge helpful discussion with Xander Tielens regarding the sputtering yield formulae used in this paper and for his constructive comments in refereeing this manuscript. This work was supported by NASA Infrared Astrophysics Theory Program under RTOP no. 188-44-53-05.

REFERENCES

Anders, E., & Grevesse, N. 1989, Geochim. Cosmochim. Acta, 53, 197
Arendt, R. G., Dwek, E., & Leisawitz, D. L. 1992, ApJ, 400, 562
Arendt, R. G., Dwek, E., & Petre, R. 1991, ApJ, 368, 474
Bohdansky, J. 1984, Nucl. Instrum. Methods Phys. Res., B2, 587
Cox, D. P., & Raymond, J. C. 1985, ApJ, 298, 651
De Boer, K. S., Jura, M. A., & Shull, J. M. 1987, in Exploring the Universe with the *IUE* Satellite, ed. Y. Kondo (Dordrecht: Reidel), 485
Draine, B. T. 1981, ApJ, 245, 880
Draine, B. T., & Anderson, N. 1985, ApJ, 292, 494
Draine, B. T., & Lee, H. M. 1984, ApJ, 258, 89
Draine, B. T., & McKee, C. F. 1993, ARA&A, 31, 373
Draine, B. T., & Salpeter, E. E. 1979, ApJ, 231, 77
Dwek, E. 1986, ApJ, 302, 363
Dwek, E., & Arendt, R. G. 1992, ARA&A, 30, 11
Dwek, E., Dinerstein, H. L., Gillett, F. C., Hauser, M. G., & Rice, W. L. 1987, ApJ, 315, 571
Dwek, E., & Scalo, J. M. 1979, ApJ, 233, L81
———. 1980, ApJ, 239, 193
Dwek, E., & Smith, R. K. 1996, ApJ, in press
Itoh, H. 1989, PASJ, 41, 853
Jones, A. P., Tielens, A. G. G. M., Hollenbach, D. J., & McKee, C. F. 1994, ApJ, 433, 797
Long, K. S., Blair, W. P., Vancura, O., Bowers, C. W., Davidsen, A. F., & Raymond, J. C. 1992, ApJ, 400, 214
Mathis, J. S., Rumpl, W., & Nordsieck, K. H. 1977, ApJ, 217, 425
McKee, C. F. 1989, in Interstellar Dust, ed. L. J. Allamandola & A. G. G. M. Tielens (Dordrecht: Kluwer), 431
McKee, C. F., Hollenbach, D. J., Seab, C. G., & Tielens, A. G. G. M. 1987, ApJ, 318, 674
Raymond, J. C. 1979, ApJS, 39, 1
Shull, J. M. 1977, ApJ, 215, 805
———. 1978, ApJ, 226, 858
Sigmund, P. 1981, in Sputtering by Particle Bombardment I, ed. R. Behrisch (Berlin: Springer-Verlag), 9
Spitzer, L. 1962, Physics of the Fully Ionized Gases (New York: Interscience)
———. 1976, Comments Astrophys., 6, 177
———. 1978, Physical Processes in the Interstellar Medium (New York: Wiley)
Taylor, G. I. 1950, Proc. R. Soc. London A, 201, 159
Tielens, A. G. G. M., McKee, C. F., Seab, G. C., & Hollenbach, D. J. 1994, ApJ, 431, 321
Vancura, O., Raymond, J. C., Dwek, E., Blair, W. P., Long, K. S., & Foster, S. M. 1994, ApJ, 431, 188